Analyst

PAPER

View Article Online
View Journal | View Issue

Cite this: *Analyst*, 2015, **140**, 6804

A local collision probability approximation for predicting momentum transfer cross sections†

Christian Bleiholder

The local collision probability approximation (LCPA) method is introduced to compute molecular momentum transfer cross sections for comparison to ion mobility experiments. The LCPA replaces the (non-local) scattering trajectory used in the trajectory method to describe the collision process by a (local) collision probability function. This momentum transfer probability is computed using the exact same analyte–buffer interaction potential as used in the trajectory method. Subsequently, the momentum transfer cross section $\Omega_{\mathrm{LCPA}}(T)$ is calculated in a projection-type manner (corrected for shape effects through a shape factor). Benchmark calculations on a set of 208 carbon clusters with a range of molecular size and degree of concavity demonstrate that LCPA and trajectory calculations agree closely with one another. The results discussed here indicate that the LCPA is suitable to efficiently calculate momentum transfer cross sections for use in ion mobility spectrometry in conjunction with different buffer gases.

Received 13th April 2015,
Accepted 9th July 2015

DOI: 10.1039/c5an00712g

www.rsc.org/analyst

Introduction

Ion mobility/mass spectrometry (IM/MS) has advanced into a powerful structure elucidation tool,[1–4] in particular when investigating a steady-state of co-existing and interconverting conformations of macromolecular compounds.[5–9] The structural analysis of an ion mobility/mass spectrometry experiment starts with determining the momentum transfer cross section $\Omega(T)$ from the reduced ion mobility K_0 (which is determined from the experiment):[10,11]

$$\Omega(T) = \frac{3ze}{16N_0}\sqrt{\frac{2\pi}{\mu k_B T}}\frac{1}{K_0} \quad (1)$$

Here, z and e are the molecular and electronic charge, respectively, N_0 the reduced gas number density, μ the reduced mass of the analyte–ion buffer gas particle pair, and T the temperature of the buffer gas. Subsequently, a possible molecular structure is guessed and its theoretical momentum transfer cross section $\Omega_{\mathrm{calc}}(T)$ is calculated.[12–14] These two steps are repeated successively until the theoretical cross section $\Omega_{\mathrm{calc}}(T)$ is considered to 'match' the experimental cross section $\Omega(T)$, in which case the structure is assigned to the experimental data. This procedure is repeated for each IM/MS peak of interest. It is obvious, therefore, that the accuracy of IM/MS-based structure analysis crucially depends on the method used to calculate the theoretical cross section.

Several methods exist to predict the cross section of an analyte in helium buffer gas.[15–22] These include the traditional projection approximation (PA)[15,19,22] and trajectory (TM)[20] methods but also the more recently developed projection superposition approximation (PSA)[17,18,23,24] and scattering on electron density isosurfaces (SEDI)[16,21] methods. These methods vary in their treatment of the collision process, with the trajectory method being the most rigorous. Projection approximation methods ignore the details of the collision process and instead treat analyte–buffer gas collisions as a probabilistic process.

While helium has traditionally been used for IMS-based structure-elucidation,[25–27] recent commercial developments[28–30] have made the use of nitrogen buffer gas common. However, developing methods to predict the momentum transfer cross section in buffer gases other than helium has largely been neglected. Two exceptions are the recent parametrizations of the PSA[31] and trajectory[32,33] methods for use with nitrogen. These two methods appear to reach their limit for practical use with nitrogen buffer gas, for different reasons. The trajectory method is even more computationally demanding for nitrogen than it is for helium[34,35] and therefore appears increasingly impractical for buffer gases that interact more strongly than helium. On the other hand, the PSA method does not directly

Department of Chemistry and Biochemistry, Florida State University, Florida State University, Tallahassee, FL 32306-4390, USA. E-mail: cbleiholder@fsu.edu

†Electronic supplementary information (ESI) available: Mathematical details of the LCPA method. Details for a reference implementation. Examples of the collision surface. Molecular surfaces used in the PSA method. Temperature-dependent cross sections (LCPA, trajectory method) and shape factors for various carbon clusters for helium and nitrogen. Comparison of Lennard-Jones parameters. Error distribution of LCPA cross sections relative to the trajectory method. Comparison of CPU times. See DOI: 10.1039/c5an00712g

account for the analyte–buffer interaction potential. Therefore, it appears that the PSA method is increasingly cumbersome to parameterize accurately for use with strongly interacting buffer gases and varying molecular charge states.[35]

Here, the local collision probability approximation (LCPA) is introduced. The LCPA replaces the (non-local) scattering trajectory used in the trajectory method to describe the collision process by a (local) collision probability function. This collision probability is computed using the exact same analyte–buffer interaction potential as used in the trajectory method. Subsequently, the momentum transfer cross section $\Omega_{\mathrm{LCPA}}(T)$ is calculated in a projection-type manner (corrected for shape effects through a shape factor). As a result, the LCPA explicitly considers the analyte–buffer gas interaction potential while being computationally efficient. In this work, the concepts fundamental to the LCPA are first presented and LCPA calculations are subsequently compared to PSA and trajectory calculations for carbon clusters.

Theory

This section develops the conceptual framework of the LCPA. To this end, the trajectory and projection approximation methods are first discussed briefly in order to provide a basis for the subsequent introduction of the LCPA. Technical details that are not essential for the conceptual understanding of the LCPA can be found in the ESI.†

Key concepts of the trajectory method

The most rigorous method available to date is the trajectory method,[20] but it's also the most computationally demanding because it simulates the physical momentum transfer process. The cross section $\Omega(T)$ arising from the force acting on the analyte ion due to collisions with the buffer gas particles can be expressed as[11]

$$\Omega(T) = \int_0^\infty f(\varepsilon, T)\Omega(\varepsilon)\mathrm{d}\varepsilon \tag{2}$$

were $\Omega(\varepsilon)$ is the microcanonical momentum transfer cross section and $f(\varepsilon, T)$ the Boltzmann distribution of the kinetic energy ε for an analyte ion–buffer gas system at temperature T. The microcanonical cross section $\Omega(\varepsilon)$ can be expressed by the deflection angle θ and the differential collision cross section $\sigma(\theta, \varepsilon)$ as

$$\Omega(\varepsilon) = 2\pi \int_0^\pi (1 - \cos\,\theta)\sigma(\varepsilon, \theta)\,\sin\,\theta\mathrm{d}\theta \tag{3}$$

Here, the term $(1 - \cos\theta)$ corresponds to the fraction of momentum transferred *via* a collision with deflection angle θ and can take on values between 0 ($\theta = 0$) and 2 ($\theta = \pi$, head-on collision).

The deflection angle θ is a complicated quantity itself and depends on the kinetic energy ε and the relative orientation $\boldsymbol{b}$ of the colliding particles. Therefore, the deflection angle θ is often[36] expressed in terms of the deflection function $\theta(\varepsilon, \boldsymbol{b})$ with

$$\theta(\varepsilon, \boldsymbol{b}) \equiv \theta[\boldsymbol{r}(t, \varepsilon, \boldsymbol{b}), U(\boldsymbol{r})] \tag{4}$$

The notation $\theta[\boldsymbol{r}(t, \varepsilon, \boldsymbol{b}), U(\boldsymbol{r})]$ is used here to emphasize two facts. First, the deflection angle $\theta(\varepsilon, \boldsymbol{b})$ is derived from a collision trajectory $\boldsymbol{r}(t, \varepsilon, \boldsymbol{b})$ (see Fig. 1). Second, the collision trajectory $\boldsymbol{r}(t, \varepsilon, \boldsymbol{b})$ is obtained by solving the equations of motions on an interaction potential $U(\boldsymbol{r})$ starting from collision geometry $\boldsymbol{b}$ with kinetic energy ε. For a spherical analyte the collision geometry $\boldsymbol{b}$ reduces to the one-dimensional impact parameter b and eqn (1) can be rewritten as

$$\Omega(T) = 2\pi \int_0^\infty f(\varepsilon, T) \int_0^\infty (1 - \cos\,\theta(\varepsilon, b))b\mathrm{d}b\mathrm{d}\varepsilon \tag{5}$$

That is the familiar form often found in the literature.[10,36] The trajectory method[20] calculates hundreds of thousands to millions of distinct collision trajectories $\boldsymbol{r}(t, \varepsilon, \boldsymbol{b})$ when estimating the integral $\Omega(T)$ in eqn (5).

What is important for the current work are two considerations. First, the trajectory method computes each trajectory $\boldsymbol{r}$

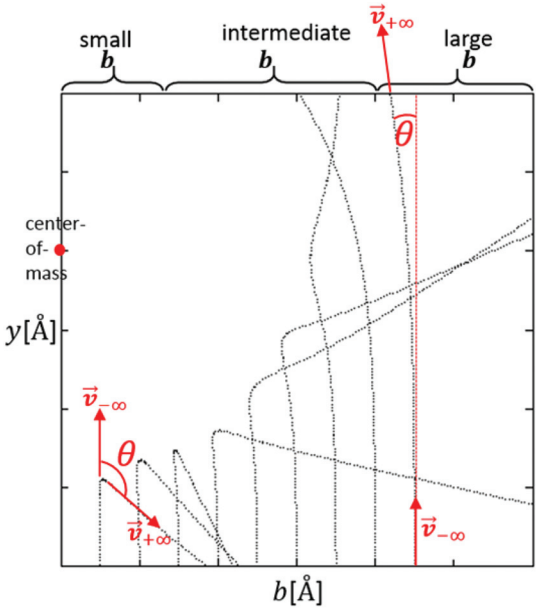

Fig. 1 Plot of some Buckminster-C_{60} – helium collision trajectories $\boldsymbol{r}(t, \varepsilon, b)$ for different impact parameters b at energy ε/k_B = 300 K. The trajectories $\boldsymbol{r}(t, \varepsilon, b)$ are the solutions to the equations of motion, integrated from time $t = -\infty$ to $t = +\infty$ for the initial value problem defined by impact parameter b and kinetic energy ε. The interaction potential $U(\boldsymbol{r})$ and its gradient $\nabla U(\boldsymbol{r})$ must be evaluated along the entire trajectory. The fraction of momentum transferred per collision trajectory is given by $1 - \cos\theta(\varepsilon, b)$, where $\theta(\varepsilon, b)$ is called the deflection angle. The deflection angle $\theta(\varepsilon, b)$ is determined for each trajectory $\boldsymbol{r}(t, \varepsilon, b)$ as the angle $\angle(\vec{v}_{t_{-\infty}}, \vec{v}_{t_{+\infty}})$ between the initial and final velocity vectors, $\vec{v}_{-\infty}$ and $\vec{v}_{+\infty}$. The deflection angle $\theta(\varepsilon, b)$, and thus the momentum transfer $1 - \theta(\varepsilon, b)$, changes with increasing impact parameter b due to the interaction potential $U(\boldsymbol{r})$. The deflection angle $\theta(\varepsilon, b)$ is particularly sensitive to $U(\boldsymbol{r})$ for intermediate impact parameters b.

(t, ε, $\boldsymbol{b}$) using a potential energy function $U(\boldsymbol{r})$ that explicitly accounts for the analyte–buffer gas interaction, such as[20]

$$U(\boldsymbol{r}) = \sum_{l=1}^{\text{atoms}} E_l \left[\left(\frac{r_{\min,l}}{|\boldsymbol{r} - \boldsymbol{R}_l|} \right)^{12} - \left(\frac{r_{\min,l}}{|\boldsymbol{r} - \boldsymbol{R}_l|} \right)^{6} \right] + V(\boldsymbol{r}) \qquad (6)$$

Here, E_l, and $r_{\min,l}$ are the Lennard-Jones parameters, $\boldsymbol{R}_l$ the centers of the atoms, and $V(\boldsymbol{r})$ is the charge-induced interaction potential between the analyte ion and the buffer gas particle. As a result, the trajectory method estimates $\Omega(T)$ accurately for different buffer gases and complicated molecular shapes.

Second, the trajectory method repeatedly integrates the equations of motions over time t on the interaction potential $U(\boldsymbol{r})$ in order to obtain each individual trajectory $\boldsymbol{r}(t, \varepsilon, \boldsymbol{b})$. Thus, the potential energy $U(\boldsymbol{r})$ and the gradient $\nabla U(\boldsymbol{r})$ must be computed *at each point* $\boldsymbol{r}$ *along the entire trajectory* $\boldsymbol{r}(t, \varepsilon, \boldsymbol{b})$ in order to obtain a single trajectory $\boldsymbol{r}(t, \varepsilon, \boldsymbol{b})$ (and the corresponding deflection angle $\theta(\varepsilon, \boldsymbol{b})$, see Fig. 1). As a consequence, the trajectory method is computationally highly demanding. *In other words, the trajectory method is computationally demanding because the deflection angle* $\theta(\varepsilon, b)$ *is a non-local function of the interaction potential* $U(r)$.

Key concepts of projection approximation methods

Projection approximation (PA) methods[17–19,22–24] estimate $\Omega(T)$ as an orientation-average $\langle \sigma(T) \rangle_n$ of axis-aligned projection cross sections $\sigma(T, \vec{z}_k)$ according to

$$\begin{aligned} \Omega(T) \approx \Omega^{\text{PA}}(T) &= \rho(T) \langle \sigma(T) \rangle_n \\ &= \rho(T) \lim_{n \to \infty} \frac{1}{n} \sum_{k=1}^{n} \sigma(T, \vec{z}_k) \end{aligned} \qquad (7)$$

Here, the averaging in $\langle \sigma(T) \rangle_n = \lim_{n \to \infty} \frac{1}{n} \sum_{k=1}^{n} \sigma(T, \vec{z}_k)$ is performed over n orientations along axes $\vec{z}_k$. The term $\rho(T)$ is called shape factor and equal to 1 in the traditional PA[15,19,22] but computed explicitly in the PSA[17,18,23,24] (see below). The axis-aligned projection cross sections $\sigma(T, \vec{z}_k)$ are given by

$$\sigma(T, \vec{z}_k) = \boldsymbol{A}_k \omega(\boldsymbol{A}_k, T) \qquad (8)$$

where $\boldsymbol{A}_k$ denotes an area on the plane perpendicular to $\vec{z}_k$ and $\omega(\boldsymbol{A}_k, T)$ is the probability for a collision to occur within the area $\boldsymbol{A}_k$ at temperature T. In practice, the probability $\omega(\boldsymbol{A}_k, T)$ is obtained for each axis $\vec{z}_k$ as

$$\omega(\boldsymbol{A}_k, T) = \frac{n_{\text{coll}}}{n_{\text{coll}} + n_{\text{miss}}} \qquad (9)$$

Here, n_{coll} and n_{miss} denote the number of points $\boldsymbol{q}$ on plane $\boldsymbol{A}_k$ that are considered a "collision" and "no collision" with the analyte ion, respectively. A collision is considered to occur at point $\boldsymbol{q}$ on plane $\boldsymbol{A}_k$ if the Monte Carlo criterion $p \leq \mathcal{P}(\boldsymbol{q}, T)$ is true, where p is a random number and $\mathcal{P}(\boldsymbol{q}, T)$ is the probability that a collision occurs at point $\boldsymbol{q}$. The main difference between different PA methods lies in the definition of $\mathcal{P}(\boldsymbol{q}, T)$. In the traditional PA method,[15,19,22] $\mathcal{P}(\boldsymbol{q}, T)$ is equal to 1 if the point (x, y) lies within a hard sphere radius of an atom, and 0 otherwise. In the PSA method,[17,18,23,24] $\mathcal{P}(\boldsymbol{q}, T)$ assumes a more complicated, exponentially-decaying form. The reader is referred to the literature for details on $\mathcal{P}(\boldsymbol{q}, T)$ employed in the PSA method,[17] but what is important for the current work are three aspects. For one, the axis-aligned projection cross sections $\sigma(T, \vec{z}_k)$ are only accurate for an analyte ion with (locally) convex molecular shape.[15,36] Thus a shape-factor $\rho(T)$ must be calculated to achieve accurate structural assignment of the experiment (see section S1.3, ESI†). Second, PA methods do not explicitly consider the analyte–buffer interaction potential $U(\boldsymbol{r})$. As a consequence, these methods are anticipated to be increasingly inaccurate when used to predict momentum transfer cross sections for molecules with a range of molecular charge distributions in strongly interacting buffer gases, such as carbon dioxide. Finally, PA methods are computationally highly efficient because *the molecular collision probability* $\mathcal{P}(\boldsymbol{q}, T)$ *is a local quantity and thus depends only on the position* $\boldsymbol{q}$.

In sum, the trajectory method estimates $\Omega(T)$ accurately largely because the interaction potential $U(\boldsymbol{r})$ is explicitly considered (as opposed to projection approximation methods). By contrast, PA methods are computationally efficient because the collision probability $\mathcal{P}(\boldsymbol{q}, T)$ is a local quantity (as opposed to the deflection angle $\theta(\varepsilon, \boldsymbol{b})$ used in the trajectory method).

Local collision probability approximation (LCPA)

The key idea of the local collision probability approximation (LCPA) is to combine aspects from the projection approximation and trajectory method. First, the momentum transfer cross section $\Omega(T)$ is computed according to eqn (2), with the microcanonical momentum transfer cross section $\Omega(\varepsilon)$ from eqn (3) estimated as

$$\Omega(\varepsilon) \approx \Omega^{\text{LCPA}}(\varepsilon) = \xi(\varepsilon) \rho(\varepsilon) \qquad (10)$$

where $\xi(\varepsilon)$ is the momentum transfer cross section at energy ε for a convex molecular shape (*i.e.* roughness, dents, or other concave parts of the analyte are ignored). This approach ensures computational efficiency because it is known that $\xi(\varepsilon)$ can be computed accurately by a projection approximation.[15,36] The quantity $\rho(\varepsilon)$ is the shape factor that captures the deviation of $\xi(\varepsilon)$ from $\Omega(\varepsilon)$ due to shape effects (see section S1.3 in the ESI† for details).[15,17,37] This Ansatz is conceptually similar to the one taken in the PSA method, which has proven to yield accurate cross sections.[17,18,23,24,34,37–39] Second, to ensure accuracy for a number of drift gases, both $\xi(\varepsilon)$ and $\rho(\varepsilon)$ are calculated directly from the interaction potential $U(\boldsymbol{r})$. Thus, the LCPA method writes both $\xi(\varepsilon)$ and $\rho(\varepsilon)$ as functionals of a collision probability function $\tau(\varepsilon, \boldsymbol{r})$, *i.e.* $\xi(\varepsilon) \equiv \xi[\tau(\varepsilon, \boldsymbol{r})]$ and $\rho(\varepsilon) \equiv \rho[\tau(\varepsilon, \boldsymbol{r})]$. What is important are two properties of the collision probability function $\tau(\varepsilon, \boldsymbol{r})$. For one, $\tau(\varepsilon, \boldsymbol{r})$ is computed directly from the interaction potential $U(\boldsymbol{r})$. This property ensures that $\tau(\varepsilon, \boldsymbol{r})$ is sensitive to the analyte shape, charge, and the nature of the buffer gas (see analysis of the trajectory method above). Second, $\tau(\varepsilon, \boldsymbol{r})$ is *local* with respect to $U(\boldsymbol{r})$ in the sense that $U(\boldsymbol{r})$ needs to be known only at the position $\boldsymbol{r}$ in order to evaluate

$\tau(\varepsilon, \boldsymbol{r})$. This property ensures that $\tau(\varepsilon, \boldsymbol{r})$ can be evaluated computationally efficiently (see the analysis of the projection approximation above). As a result, $\Omega(T)$ is evaluated computationally efficiently while explicitly taking into account the analyte ion–buffer gas interaction potential $U(\boldsymbol{r})$.

The local collision probability function $\tau(\varepsilon, \boldsymbol{r})$ corresponds to the probability that a collision occurs at position $\boldsymbol{r}$ with kinetic energy ε when a buffer gas particle approaches the analyte along a ray. As pointed out,[38] "the quantity which ultimately determines whether a collision between two particles took place or not is the scattering angle", $\theta(\varepsilon, \boldsymbol{b})$. This is so because the transfer of momentum (*i.e.* force) arising from the collision is determined by the change in direction of the velocities of the two particles involved (Fig. 1).[11,36] Qualitatively, constructing $\tau(\varepsilon, \boldsymbol{r})$ is intuitive: if only a small amount of momentum $1 - \cos\theta(\varepsilon, \boldsymbol{b})$ is transferred *via* a collision (*i.e.* small deflection angle $\theta(\varepsilon, \boldsymbol{b})$, see Fig. 1)[36] then the collision probability $\tau(\varepsilon, \boldsymbol{r})$ should take on a small value, and *vice versa*. It is further intuitive that the collision probability $\tau(\varepsilon, \boldsymbol{r})$ and deflection angle $\theta(\varepsilon, \boldsymbol{b})$ of glancing collisions (*i.e.* large values of $\boldsymbol{b}$) decrease with increasing ratio $\varepsilon/U(\boldsymbol{r})$ between the kinetic energy ε and the interaction potential $U(\boldsymbol{r})$, and *vice versa*.[36] Further, the transferred momentum and deflection angle $\theta(\varepsilon, \boldsymbol{b})$ of head-on-collisions (*i.e.* small values of $\boldsymbol{b}$) should only depend marginally on the ratio $\varepsilon/U(\boldsymbol{r})$.

A mathematical expression for $\tau(\varepsilon, \boldsymbol{r})$ can be constructed when considering that the interaction potential $U(\boldsymbol{r})$ can be written as an integral over delta-potentials (see ESI† for details). Therefore, the local collision probability $\tau(\varepsilon, \boldsymbol{r})$ is expressed here as the reflection coefficient R when a matter wave with kinetic energy ε and reduced mass μ moving along a ray is scattered at a delta potential with height equal to the potential $U(\boldsymbol{r})$ at position $\boldsymbol{r}$ (see Fig. S1, ESI†). Conceptually, this amounts to saying that collisions are more likely to occur at positions $\boldsymbol{r}$ that are close to the ion (head-on collisions where the interaction potential $U(\boldsymbol{r})$ is strongly repulsive) but less likely to occur at larger distances to the ion (where the interaction potential $U(\boldsymbol{r})$ is slightly attractive). As described in more detail in the ESI,† $\tau(\varepsilon, \boldsymbol{r})$ can then be expressed as

$$\tau(\varepsilon, \boldsymbol{r}) = \frac{1}{1 + \left[\frac{\varepsilon}{\pi U(\boldsymbol{r})}\right]^2} \tag{11}$$

where ε is the kinetic energy of the collision process and $U(\boldsymbol{r})$ the interaction potential.

It is now briefly discussed how the convex microcanonical cross section $\xi(\varepsilon)$ and shape factor $\rho(\varepsilon)$ may be constructed from $\tau(\varepsilon, \boldsymbol{r})$. For clarity, the interested reader is referred to section S1, ESI,† for more technical details. The key aspect of constructing both $\xi(\varepsilon)$ and $\rho(\varepsilon)$ from $\tau(\varepsilon, \boldsymbol{r})$ is to first determine a collision surface $\mathcal{S}$. The collision surface $\mathcal{S}$ represents the set of points $\boldsymbol{r}$ in space at which a collision is considered to occur (see Fig. S1 in the ESI†). Many approaches to determining the collision surface $\mathcal{S}$ are conceivable. Currently, $\mathcal{S}$ is obtained by casting a ray $\boldsymbol{r}(s) = \boldsymbol{r}_\infty + s\boldsymbol{z}$ from point $\boldsymbol{r}_\infty$ far way from the molecular center-of-mass along direction $\boldsymbol{z}$ onto the molecule. A collision is then considered to occur when the Monte-Carlo-criterion $p \leq \tau(\varepsilon, \boldsymbol{r}(s))$ is true, where p is a random number. A large number of rays are cast to determine the vertices of the surface $\mathcal{S}$ (Fig. S2 in the ESI†). The corresponding edges of the surface $\mathcal{S}$ can be determined by standard surface reconstruction algorithms. The current implementation uses a Delaunay triangulation[40]-based method using the 'qhull' algorithm[41] but other techniques, such as marching cubes[42] or Poisson surface reconstruction[43] methods, have also been used during the development process. Once the vertices and edges of the collision surface $\mathcal{S}$ are known (see Fig. S2 in the ESI†), the microcanonical cross section $\xi(\varepsilon)$ and shape factor $\rho(\varepsilon)$ can easily be calculated by known procedures.[17,19,22,37] In the current implementation, the cross section $\xi(\varepsilon)$ is calculated as the orientation-averaged projection area of the collision surface $\mathcal{S}$ and the shape factor $\rho(\varepsilon) = \Omega(\varepsilon)/\xi(\varepsilon)$ is estimated as

$$\rho(\varepsilon) \approx \frac{A_{\mathcal{S}}}{A_{\mathrm{ce}}} \tag{12}$$

where A_S and A_{ce} are the surface areas of the collision surface $\mathcal{S}$ and the convex envelope of $\mathcal{S}$, respectively. This estimate of the shape factor is appropriate for the molecular shapes discussed in this work but may be modified for wider applicability (see ESI† section S1.3 for details).[17,18,23,24,34,37–39] Once $\xi(\varepsilon)$ and $\rho(\varepsilon)$ are known, the momentum transfer cross sections $\Omega(\varepsilon)$ and $\Omega(T)$ can be computed *via* eqn (10) and (2). A detailed description of the reference LCPA implementation used in this work can be found in the ESI.†

Discussion

Comparison between the functions $\tau(\varepsilon, \boldsymbol{r})$, $\mathcal{P}(q, T)$, and $\theta(\varepsilon, \boldsymbol{b})$ used in the LCPA, PSA, and trajectory methods

The relative momentum transferred when two particles collide is given by $1 - \cos\theta(\varepsilon, \boldsymbol{b})$, where $\theta(\varepsilon, \boldsymbol{b})$ is the deflection angle.[11,36] Therefore, the deflection angle $\theta(\varepsilon, \boldsymbol{b})$ and the local collision probability $\tau(\varepsilon, \boldsymbol{r})$ are intrinsically related to each other. Further, both $\theta(\varepsilon, \boldsymbol{b})$ and $\tau(\varepsilon, \boldsymbol{r})$ depend directly on the potential energy $U(\boldsymbol{r})$ (eqn (4) and (11), respectively). Fig. 2a shows the potential energy $U(\boldsymbol{r})$ as a function of the distance $\boldsymbol{r}$ for Buckminster-C_{60}.[44] The corresponding Lennard-Jones parameters (E = 0.0309 kcal mol^{-1} and $r_{\min}$ = 3.405 Å) are taken from the trajectory method.[20] The resulting momentum transfer probability function $\tau(\varepsilon, \boldsymbol{r})$ is plotted in Fig. 2b for three different kinetic energies (ε/k_B = 300 K, 600 K, and 3000 K). It is noted that $\tau(\varepsilon, \boldsymbol{r})$ approaches 1 for $\boldsymbol{r} \to 0$. This observation reflects the large momentum transfer $1 - \cos\theta(\varepsilon, \boldsymbol{b})$ due to head-on collisions (*i.e.* large deflection angles $\theta(\varepsilon, \boldsymbol{b})$) for small impact parameters b (Fig. 1). Further, $\tau(\varepsilon, \boldsymbol{r})$ approaches 0 for $\boldsymbol{r} \to \infty$. This behavior of $\tau(\varepsilon, \boldsymbol{r})$ reflects the decreasing amount of momentum transfer due to glancing collisions (*i.e.* small deflection angles $\theta(\varepsilon, \boldsymbol{b})$) for large impact parameters b (Fig. 1). It is emphasized that the collision probability $\tau(\varepsilon, \boldsymbol{r})$ in Fig. 2 is still significant at large distances $|\boldsymbol{r}|$, even at 300 K. This observation indicates that the ion–neutral interactions taking place

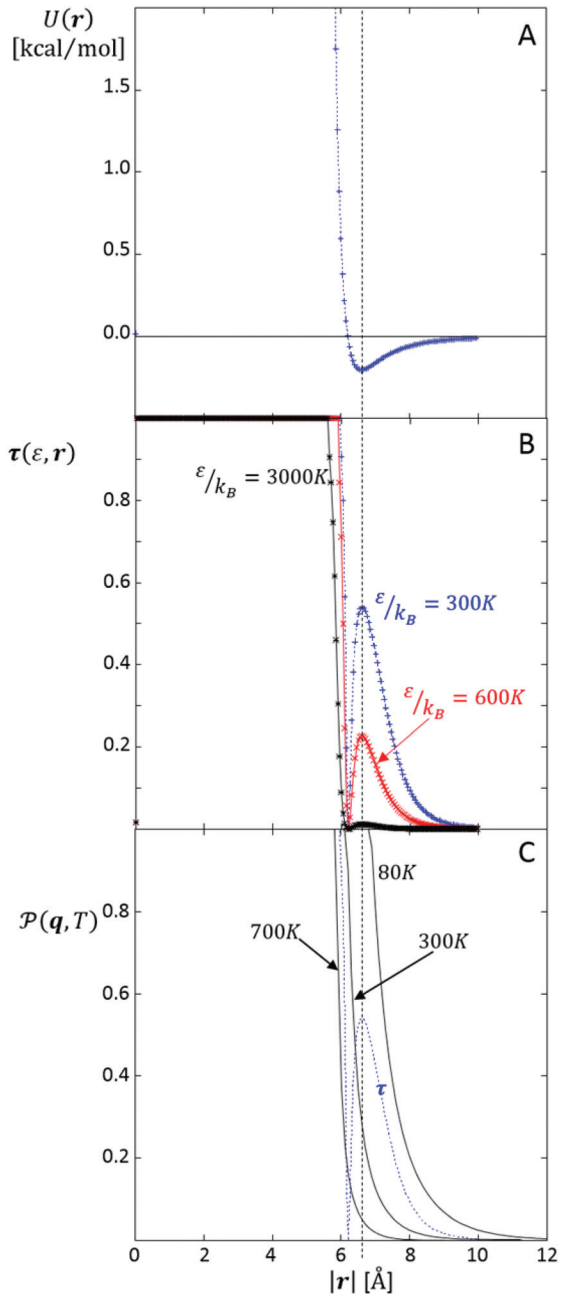

Fig. 2 Interaction potential $U(r)$, local collision probability $\tau(\varepsilon, \boldsymbol{r})$, and collision probability $\mathcal{P}(T, \boldsymbol{q})$ for C_{60}. (A) Plotted is the interaction potential $U(\boldsymbol{r})$ for C_{60} using eqn (6) with reported parameters.[20] (B) Local collision probability $\tau(\varepsilon, \boldsymbol{r})$ used in the LCPA method for three different energies ε/k_B. Clearly visible is a local maximum at the position r_{min} where $U(\boldsymbol{r})$ is minimal. Further, the height of the local maximum decreases with increasing energy ε. (C) Molecular collision probability $\mathcal{P}(T, \boldsymbol{r})$ used in the PSA method. The figure shows that $\mathcal{P}(T, \boldsymbol{r})$ monotonically decreases with increasing distance, without going through a local maximum. Local collision probability $\tau(\varepsilon = 300\ \text{K}\ k_B, \boldsymbol{r})$ is included for comparison (dotted).

at long ranges are intrinsically represented by the LCPA. Additionally, the plot shows that $\tau(\varepsilon, \boldsymbol{r})$ decays faster for higher kinetic energies ε. This observation reflects the decrease in the deflection angle $\theta(\varepsilon, \boldsymbol{b})$ for glancing collisions occurring at higher kinetic energy.[36] Overall, these observations show that $\tau(\varepsilon, \boldsymbol{r})$ correctly reflects the asymptotic behavior expected for the deflection angle $\theta(\varepsilon, \boldsymbol{b})$.[36] What is more important, however, is the behavior of $\tau(\varepsilon, \boldsymbol{r})$ in the region of intermediate impact parameters where $\theta(\varepsilon, \boldsymbol{b})$ is governed by the attractive well of the Lennard-Jones potential.[36] Fig. 2b shows that $\tau(\varepsilon, \boldsymbol{r})$ displays a local maximum at the distance r_{min} where $U(\boldsymbol{r})$ is minimal. The figure also shows that the height of this local maximum decreases with increasing energy ε. These two observations take on increased significance because it is known[36] that the deflection angle $\theta(\varepsilon, \boldsymbol{b})$ goes through a minimum (and thus the momentum transfer $1 - \cos\theta(\varepsilon, \boldsymbol{b})$ through a local maximum) at impact parameter $\boldsymbol{b}_r$ where $\theta(\varepsilon, \boldsymbol{b}_r)$ is called the rainbow angle. It is further known from the impulse approximation[36] that the rainbow angle, and thus the momentum transferred, decreases with increasing ratio $\varepsilon/U(\boldsymbol{b}_r)$. Thus, Fig. 2b shows that $\tau(\varepsilon, \boldsymbol{r})$ correctly reproduces the properties of the rainbow angle $\theta(\varepsilon, \boldsymbol{b}_r)$. In sum, the data indicate that $\tau(\varepsilon, \boldsymbol{r})$ correctly reflects the momentum transfer expected from the deflection angle $\theta(\varepsilon, \boldsymbol{b}_r)$, at least on a qualitative basis.

The local collision probability $\tau(\varepsilon, \boldsymbol{r})$ of the LCPA method is further related to the molecular collision probability $\mathcal{P}(\boldsymbol{q}, T)$ of the PSA method: both quantities are a measure of the likelihood for a collision to occur at a specific position in space. (Please note that while $\tau(\varepsilon, \boldsymbol{r})$ is defined in three dimensions with $\boldsymbol{r} = (x, y, z)$, $\mathcal{P}(\boldsymbol{q}, T)$ is defined in only two dimensions with $\boldsymbol{q} = (x, y)$. However, z can be set equal to 0 and thus $\boldsymbol{q} = \boldsymbol{r}$ $(x, y, 0)$ for the sake of argument.) Therefore, comparing $\tau(\varepsilon, \boldsymbol{r})$ and $\mathcal{P}(\boldsymbol{q}, T)$ reveals the differences in how the LCPA and PSA methods treat the collision process. Fig. 2c displays the collision probability $\mathcal{P}(\boldsymbol{q}, T)$ of the PSA method as a function of the position $\boldsymbol{q}$ for Buckminster-C_{60} at temperatures T = 80 K, 300 K, 700 K. The figure shows that $\mathcal{P}(\boldsymbol{q}, T)$ decreases monotonically from 1.0 with increasing distance $\boldsymbol{q}$. Further, $\mathcal{P}(\boldsymbol{q}, T)$ decays faster for higher temperatures. Following the discussion in the previous section, $\mathcal{P}(\boldsymbol{q}, T)$ therefore correctly reflects the asymptotic behavior of the momentum transfer $1 - \cos\theta(\varepsilon, \boldsymbol{b})$ with increasing impact parameter $\boldsymbol{b}$ and kinetic energy ε. However, it is revealing to take a closer look at the region of intermediate impact parameters $\boldsymbol{b}$. Here, a local maximum (*i.e.* rainbow angle $\theta(\varepsilon, \boldsymbol{b}_r)$, see Discussion in the preceding paragraph) is expected but not observed for $\mathcal{P}(\boldsymbol{q}, T)$ in Fig. 2c. The plot thus clearly shows that $\mathcal{P}(\boldsymbol{q}, T)$ does not correctly reflect the momentum transfer $1 - \cos\theta(\varepsilon, \boldsymbol{b})$ when the attractive well of the interaction potential $U(\boldsymbol{r})$ dominates the collision process. Indeed, the collision probability $\mathcal{P}(\boldsymbol{q}, T)$ corresponds to the correct momentum transfer $1 - \cos\theta(\varepsilon, \boldsymbol{b})$ only for an entirely repulsive potential $U(\boldsymbol{r})$.[36]

In sum, the above analysis indicates that the PSA method implicitly assumes an entirely repulsive interaction potential between the analyte ion and the buffer gas particle. This assumption can certainly be made for macromolecular compounds measured in helium buffer gas: helium interacts very weakly[10] and is only marginally polarizable.[11] This was the

analyte ion–buffer gas combination that the PSA had originally been designed for.[17] However, it is anticipated that the PSA becomes increasingly inaccurate for (strongly charged) analyte ions in buffer gases with dipole or quadrupole moments, such as CO_2. By contrast, the data presented here demonstrate that the local collision probability $\tau(\varepsilon, \boldsymbol{r})$ employed in the LCPA method correctly reflects the momentum transfer $1 - \cos\theta(\varepsilon, \boldsymbol{b})$ expected from an attractive ion–neutral interaction potential $U(\boldsymbol{r})$. Thus, the LCPA method is expected to afford a significantly greater flexibility than the PSA method in terms of the buffer gas it can be accurately parameterized for.

Comparison of cross sections predicted by the LCPA, PSA, and trajectory methods for carbon clusters in helium buffer gas

This section serves to investigate whether the concepts described in the previous section result in meaningful momentum transfer cross sections $\Omega(T)$. To this end, cross sections $\Omega_{\mathrm{LCPA}}(T)$ calculated by the LCPA are compared to trajectory method cross sections $\Omega_{\mathrm{TJM}}(T)$. The exact same Lennard-Jones parameters are used for both methods (E = 0.0309 kcal mol^{-1} and $r_{\min}$ = 3.405 Å).[20] It is emphasized that these Lennard-Jones parameters were optimized to reproduce the experimental ion mobility of C_{60} with the trajectory method and are not optimized for use with the LCPA. However, it is the aim of the current work to identify how closely the LCPA method agrees with the physically more rigorous trajectory method, and thus identical parameters are chosen for both methods here.

Fig. 3 compares LCPA to trajectory method cross sections for C_{60} and C_{960} in the temperature range from 80 K to 700 K. The data reveal that the LCPA overestimates the trajectory method cross section by up to approximately 6% for C_{60}. This deviation decreases successively with increasing molecular size from C_{180} to C_{240} and C_{960} (4%, 3%, and 1%, deviation; see Fig. 3b and S4, S5 in the ESI†). Shape effects are unable to explain this trend, because the shape factor $\rho^{\mathrm{LCPA}}(T)$ is in the order of 1 for these systems (see Fig. S3–S5 in the ESI†). Instead, the observed discrepancy can be rationalized by differences between the two methods in treating the interaction potential $U(\boldsymbol{r})$. Lennard-Jones parameters E and $r_{\min}$ can be fitted for the LCPA method to reproduce the trajectory method C_{60} cross sections (E_{opt} = 0.0347 kcal mol^{-1} and $r_{\mathrm{opt,\ min}}$ = 3.21 Å, Fig. 2a). Indeed, the repulsive wall in the LCPA-optimized potential is shifted to smaller distances than in the parameters optimized for the trajectory method (Fig. S7 in the ESI†). Nevertheless, the fitted LCPA parameters still agree closely to those fitted for the trajectory method and those deduced for carbon from the interlayer interactions in graphite using combination rules (E = 0.0337 kcal mol^{-1} and $r_{\min}$ = 3.34 Å).[20]

It is further noted that the LCPA method reproduces well the trajectory method cross sections for the cups derived from C_{60}, C_{180}, C_{240}, and C_{960} (Fig. 3c and S3–S5 in the ESI,† using the trajectory method interaction potential). Here, the LCPA cross sections deviate less than 5% from the prediction made by the trajectory method in the entire temperature range studied and the two methods strongly agree for the cups of C_{240} and C_{960}. The overall agreement between the cross sections computed by the LCPA and trajectory methods can further be determined from the distribution of the relative deviation $|\Omega^{\mathrm{LCPA}} - \Omega^{\mathrm{TJM}}|/\Omega^{\mathrm{TJM}}$. LCPA cross sections were computed in the temperature range from 80 to 700 K for the same set of 208 carbon clusters used to benchmark the PSA method. The resulting error distribution can be found in Fig. S6 (ESI†). The 90% quantile of 6.1% deviation indicates that the accuracy of the LCPA method is comparable to the PSA method. However, the difference being that seven carbon parameters had been fit for the PSA method while only two, non-optimized parameters are used here for the LCPA method. The C_{60}-optimized Lennard-Jones parameters for the LCPA method

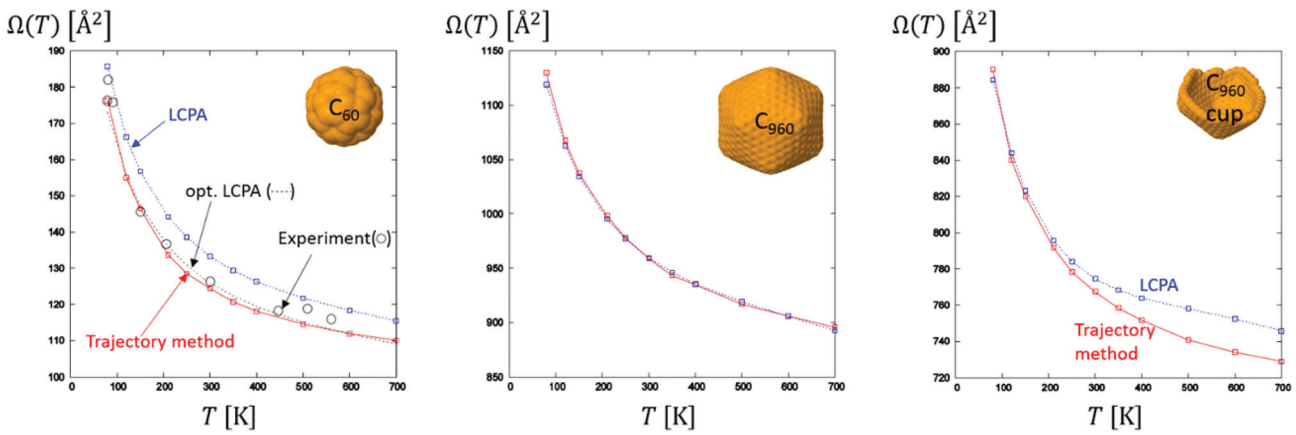

Fig. 3 Cross sections $\Omega(T)$ for C_{60}, C_{960}, and the cup of C_{960} as a function of temperature from 80 K to 700 K. LCPA cross sections were computed using the trajectory method potential (LCPA) and a potential optimized for the LCPA method (opt. LCPA). Experimental C_{60} data were taken from the literature.[22] An overall strong agreement among the LCPA and trajectory methods is visible, with the only exception being the LCPA calculations for C_{60} when the trajectory method potential is used (~5% deviation). However, both methods perform comparable when compared to the experimental values.

improve the agreement to the trajectory method slightly (90% quantile of 4.9%, Fig. S6 in the ESI†).

Comparison of cross sections predicted by the LCPA, PSA, and trajectory methods for carbon clusters in nitrogen buffer gas

In order to assess the ability of the LCPA to accurately compute cross sections in electronically different buffer gases, LCPA cross sections are compared to PSA and trajectory method cross section for nitrogen. Trajectory method cross sections were calculated using the recent modification for use with nitrogen buffer gas.[32,33] Nitrogen parameters were estimated for the LCPA method by the combination rules described by Lorentz[45] and Berthelot[46] from the published helium and nitrogen parameters.[10,20] (for details see Section S3 in the ESI†). It is important to point out that the nitrogen–carbon interaction potentials used in the LCPA and trajectory methods differ from each other. Consequently, the LCPA and trajectory methods are not expected to predict identical cross sections, and the comparison of nitrogen cross sections is thus discussed in a more qualitative manner here (see the discussion in section S3, ESI,† for details).

Fig. S8–S10 in the ESI† show that the LCPA method reproduces the differences between helium and nitrogen cross sections predicted by the trajectory method well. Further, for C_{240}, C_{960}, and the corresponding cups, the nitrogen cross sections predicted by the two methods agree in the order of less than 3% on average (see Fig. S9 and S10 in the ESI†). These observations support the validity of the assumptions made in the LCPA method.

Comparison of the LCPA and trajectory methods for solid and hollow carbon clusters in helium buffer gas

One major shortcoming of traditional hard-sphere methods is that long-range effects of the interaction potential are either entirely ignored[15,19] or only indirectly accounted for.[22] These long-range interactions become important when analyte ions differ in their internal structure, such as solid and hollow carbon clusters.[17] The trajectory method explicitly considers the molecular interaction potential $U(\boldsymbol{r})$ (eqn (6)) and gives larger cross sections for the solid than for the hollow clusters. By contrast, hard-sphere methods ignore the internal molecular structure and give similar cross sections for the hollow and solid clusters. One significant improvement introduced in the PSA method was to directly account for these long-range interactions through a superposition effect.[17] For this reason, PSA cross sections for the solid clusters were consistently larger than those for the hollow clusters. Thus, the PSA method was able to qualitatively reproduce the trends observed by the trajectory method. Fig. 4 plots the ratio $\Omega_{solid}/\Omega_{hollow}$ of cross sections for solid and hollow carbon clusters predicted by the LCPA, PSA, and trajectory methods as a function of temperature. As reported earlier,[17] the trajectory method predicts the solid clusters to be consistently larger than the hollow clusters. This effect is more noticeable for lower temperatures, where the solid clusters are up to 8 and 10% larger in cross section than the hollow ones. The figure shows that the PSA method agrees with the trajectory method data on a qualitative but not on a numerical level, in agreement with previous data.[17] (The only exception to this is seen for the smallest cluster (Fig. 4c) where both methods compute the absolute difference in cross section $\Omega_{solid} - \Omega_{hollow} \approx 3$ Å^2) Fig. 4 further shows that the LCPA data agree with the trajectory method within 1% over the entire temperature range studied. Thus, the data demonstrate that the LCPA method is able to numerically reproduce the effects of internal structure observed by the trajectory method for solid and hollow carbon clusters.

Comparison of the shape factors predicted by the LCPA and PSA methods for carbon clusters in helium buffer gas

The LCPA and PSA methods both employ a shape factor ρ to take into account surface roughness and concave parts of a molecular shape (see also section S1.3 in the ESI†). For the sake of comparison, a temperature-dependent shape factor $\rho^{LCPA}(T)$ can be defined for the LCPA method according to

$$\rho^{LCPA}(T) = \frac{\int_0^\infty f(\varepsilon, T)\xi(\varepsilon)\rho(\varepsilon)\mathrm{d}\varepsilon}{\int_0^\infty f(\varepsilon, T)\xi(\varepsilon)\mathrm{d}\varepsilon} \quad (13)$$

Fig. 5 compares the shape factors $\rho(T)$ predicted by the LCPA and PSA methods in the temperature range from 80 K to 700 K for C_{60}, C_{240}, and C_{960} to those of their corresponding cups. Several observations can be made. First, it is noted that both methods predict the shape factors close to 1.0 for the convex shapes C_{60}, C_{240} and C_{960}. Further, the shape factors increasingly deviate from 1.0 for the corresponding cups when going from C_{60}, to C_{240} and C_{960}. These observations agree with previous reports on the shape effects of carbon clusters.[15,17] However, Fig. 5 also points out two main differences between the LCPA and PSA shape factors. First, the PSA shape factor $\rho^{PSA}(T)$ fluctuates somewhat when the temperature is changed. This observation is particularly visible for the system C_{60} where the shape factor $\rho^{PSA}(T)$ is small. While this behaviour is not expected to significantly impact the overall PSA cross section, especially for macromolecular systems the PSA method was designed for, it does point to an issue of numerical stability in the computation of the PSA shape factor $\rho^{PSA}(T)$. By contrast, the LCPA shape factor $\rho^{LCPA}(T)$ increases monotonically with increasing temperature, indicating a strong degree of numerical stability in computing $\rho^{LCPA}(T)$. Second, the PSA shape factor $\rho^{PSA}(T)$ is larger than the LCPA shape factor $\rho^{LCPA}(T)$, especially for lower temperatures. Both observations can be rationalized on the basis of using the molecular surface for the PSA shape factor calculations.[17] The molecular surface[47] is generated from hard-spheres with defined radii as input. Therefore, the PSA shape factor $\rho^{PSA}(T)$ does not directly account for the attractive well of the interaction potential and atomic superposition effects. By contrast, the collision surface $\mathcal{S}$ used in the LCPA method is based on the momentum transfer probability function $\tau(\varepsilon, \boldsymbol{r})$ and thus takes full account of the attractive portion of the potential and superposition effects through eqn (6) and (11). Two consequences follow. First, the molecular surface used in the PSA

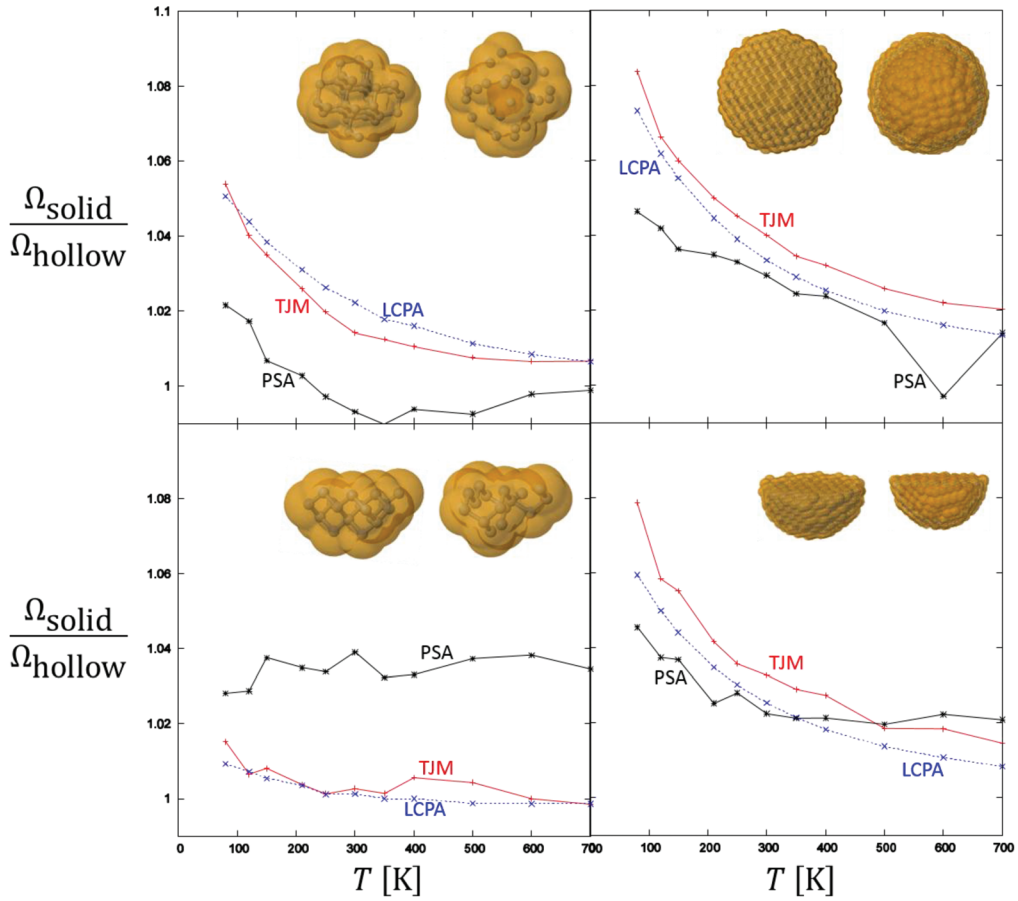

Fig. 4 Ratio $\Omega_{solid}/\Omega_{hallow}$ of cross section for solid and hollow carbon clusters with diamond-like lattice grid predicted by the LCPA, PSA, and trajectory methods. All methods predict a ratio $\Omega_{solid}/\Omega_{hallow}$ consistently greater than 1, reflecting the internal structure of the solid clusters. While the PSA data agree with the trajectory calculations on a qualitative basis, but disagree at a numerical level. By contrast, LCPA predictions achieve an almost numerical agreement with the trajectory method.

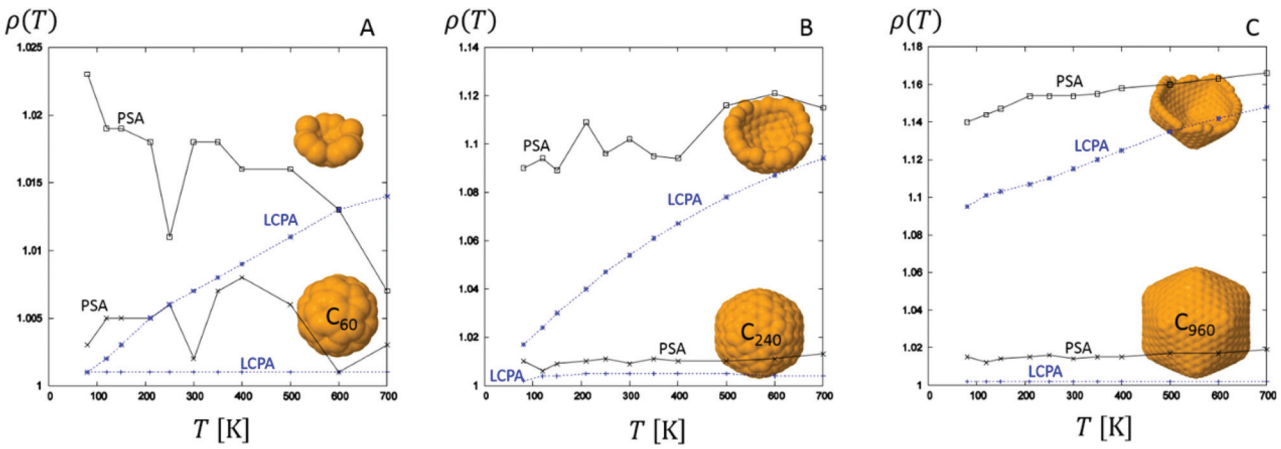

Fig. 5 Shape factors $\rho(T)$ predicted by the LCPA and PSA methods for (A) C_{60}, (B) C_{240}, (C) C_{960}, and their corresponding cups. Both methods predict $\rho(T) \approx 1$ for the fullerenes but $\rho(T) > 1$ for the cups. Both methods agree that the shape factors $\rho(T)$ increase for the cups with increasing temperature T. The PSA shape factor $\rho^{PSA}(T)$ fluctuates in the order of 1%, in particular when $\rho^{PSA}(T)$s small. By constrast, the LCPA shape factor $\rho^{LCPA}(T)$ is a smooth, monotonically increasing function of the temperature T.

calculations (see Fig. S13 in the ESI†) is rougher than the collision surface $\mathcal{S}$ (see Fig. S2 in the ESI†) used in the LCPA method. Second, the collision surface $\mathcal{S}$ strongly accounts for superposition effects of the interaction potential. Consequently, the collision surface $\mathcal{S}$ of the LCPA method appears more convex than the molecular surface used in the PSA method (see Fig. S2 and S13 in the ESI†), in particular at lower temperatures.

Comparison of CPU times used by LCPA and PSA methods

Fig. S12 (see ESI section S4† for details) compares the CPU time demand of the LCPA and PSA methods. The comparison of CPU times shows that both methods require a comparable amount of time to calculate helium cross sections. However, the PSA method is shown more demanding than the LCPA method in terms of the CPU time needed to calculate nitrogen cross sections.

Conclusions

The local collision probability approximation (LCPA) was introduced, a novel computational method to compute molecular momentum transfer cross sections $\Omega(T)$. The LCPA uses the analyte ion–buffer gas particle interaction potential to calculate a local collision probability, $\tau(\varepsilon, \boldsymbol{r})$. Subsequently, this local collision probability $\tau(\varepsilon, \boldsymbol{r})$ is used to determine a collision surface, $\mathcal{S}$. On the basis of this collision surface $\mathcal{S}$, the microcanonical cross section $\Omega(\varepsilon)$ is calculated and finally convoluted with the Boltzmann energy distribution to give the momentum transfer cross section $\Omega(T)$. One significant result of the current study is that the local collision probability $\tau(\varepsilon, \boldsymbol{r})$ is shown to qualitatively reproduce the scattering effects arising from the attractive well of the interaction potential (*i.e.* rainbow angle). The accuracy of the LCPA was assessed by comparison to the trajectory method for carbon clusters in the temperature range from 80 K to 700 K. The data reveal that the LCPA reproduce the trajectory calculations well, using the identical interaction potential optimized for the trajectory method. Further, the calculations indicate that the LCPA affords a much greater flexibility in terms of the nature of the buffer gas than the PSA method at comparable computational cost. These results indicate that the LCPA method is a promising method to efficiently calculate momentum transfer cross sections for use in ion mobility spectrometry.

Acknowledgements

C. B. thanks Thomas Wyttenbach for valuable feedback on the manuscript and the Florida State University for start-up funds.

Notes and references

1 G. von Helden, N. G. Gotts and M. T. Bowers, *Nature*, 1993, **363**, 60–63.
2 C. S. Hoaglund-Hyzer, A. E. Counterman and D. E. Clemmer, *Chem. Rev.*, 1999, **99**, 3037–3080.
3 K.-M. Ho, A. A. Shvartsburg, B. Pan, Z.-Y. Lu, C.-Z. Wang, J. G. Wacker, J. L. Fye and M. F. Jarrold, *Nature*, 1998, **392**, 582–585.
4 M. T. Bowers, P. R. Kemper, G. von Helden and P. A. M. van Koppen, *Science*, 1993, **260**, 1446–1451.
5 S. L. Bernstein, N. F. Dupuis, N. D. Lazo, T. Wyttenbach, M. M. Condron, G. Bitan, D. B. Teplow, J.-E. Shea, B. T. Ruotolo, C. V. Robinson and M. T. Bowers, *Nat. Chem.*, 2009, **1**, 326–331.
6 C. Bleiholder, N. F. Dupuis, T. Wyttenbach and M. T. Bowers, *Nat. Chem.*, 2011, **3**, 172–177.
7 C. Uetrecht, I. M. Barbu, G. K. Shoemaker, E. van Duijn and A. J. R. Heck, *Nat. Chem.*, 2011, **3**, 126–132.
8 B. T. Ruotolo, K. Giles, I. Campuzano, A. M. Sandercock, R. H. Bateman and C. V. Robinson, *Science*, 2005, **310**, 1658–1661.
9 M. Zhou, A. Politis, R. B. Davies, I. Liko, K.-J. Wu, A. G. Stewart, D. Stock and C. V. Robinson, *Nat. Chem.*, 2014, **6**, 208–215.
10 J. O. Hirschfelder, C. F. Curtiss and R. B. Bird, *Molecular Theory of Gases and Liquids*, Wiley, New York, 1954.
11 E. A. Mason and E. W. McDaniel, *Transport Properties of Ions in Gases*, Wiley, New York, 1988.
12 N. F. Dupuis, C. Wu, J.-E. Shea and M. T. Bowers, *J. Am. Chem. Soc.*, 2009, **131**, 18283–18292.
13 Y. Mao, J. Woenckhaus, J. Kolafa, M. A. Ratner and M. F. Jarrold, *J. Am. Chem. Soc.*, 1999, **121**, 2712–2721.
14 B. T. Ruotolo, J. L. P. Benesch, A. M. Sandercock, S.-J. Hyung and C. V. Robinson, *Nat. Protoc.*, 2008, **3**, 1139–1152.
15 A. A. Shvartsburg and M. F. Jarrold, *Chem. Phys. Lett.*, 1996, **261**, 86–91.
16 Y. Alexeev, D. G. Fedorov and A. A. Shvartsburg, *J. Phys. Chem. A*, 2014, **118**, 6763–6772.
17 C. Bleiholder, T. Wyttenbach and M. T. Bowers, *Int. J. Mass Spectrom.*, 2011, **308**, 1–10.
18 C. Bleiholder, S. Contreras, T. D. Do and M. T. Bowers, *Int. J. Mass Spectrom.*, 2013, **345–347**, 89–96.
19 G. von Helden, M. T. Hsu, N. Gotts and M. T. Bowers, *J. Phys. Chem.*, 1993, **97**, 8182–8192.
20 M. F. Mesleh, J. M. Hunter, A. A. Shvartsburg, G. C. Schatz and M. F. Jarrold, *J. Phys. Chem.*, 1996, **100**, 16082–16086.
21 A. A. Shvartsburg, B. Liu, M. F. Jarrold and K.-M. Ho, *J. Chem. Phys.*, 2000, **112**, 4517–4526.
22 T. Wyttenbach, G. von Helden, J. J. Batka, D. Carlat and M. T. Bowers, *J. Am. Soc. Mass Spectrom.*, 1997, **8**, 275–282.
23 S. E. Anderson, C. Bleiholder, E. R. Brocker, P. J. Stang and M. T. Bowers, *Int. J. Mass Spectrom.*, 2012, **330–332**, 78–84.
24 C. Bleiholder, S. Contreras and M. T. Bowers, *Int. J. Mass Spectrom.*, 2013, **354–355**, 275–280.
25 K. B. Shelimov and M. F. Jarrold, *J. Am. Chem. Soc.*, 1996, **118**, 1139–1147.
26 P. R. Kemper, N. F. Dupuis and M. T. Bowers, *Int. J. Mass Spectrom.*, 2009, **287**, 46–57.

27 T. Wyttenbach, P. R. Kemper and M. T. Bowers, *Int. J. Mass Spectrom.*, 2001, **212**, 13–23.
28 F. Fernandez-Lima, D. A. Kaplan, J. Suetering and M. A. Park, *Int. J. Ion Mobil. Spectrom.*, 2011, **14**, 93–98.
29 J. C. May, C. R. Goodwin, N. M. Lareau, K. L. Leaptrot, C. B. Morris, R. T. Kurulugama, A. Mordehai, C. Klein, W. Barry, E. Darland, G. Overney, K. Imatani, G. C. Stafford, J. C. Fjeldsted and J. A. McLean, *Anal. Chem.*, 2014, **86**, 2107–2116.
30 S. D. Pringle, K. Giles, J. L. Wildgoose, J. P. Williams, S. E. Slade, K. Thalassinos, R. H. Bateman, M. T. Bowers and J. H. Scrivens, *Int. J. Mass Spectrom.*, 2007, **261**, 1–12.
31 C. Bleiholder, N. R. Johnson, S. Contreras, T. Wyttenbach and M. T. Bowers, *Anal. Chem.*, 2015, DOI: 10.1021/acs.analchem.5b01429.
32 H. Kim, H. I. Kim, P. V. Johnson, L. W. Beegle, J. L. Beauchamp, W. A. Goddard and I. Kanik, *Anal. Chem.*, 2008, **80**, 1928–1936.
33 I. Campuzano, M. F. Bush, C. V. Robinson, C. Beaumont, K. Richardson, H. Kim and H. I. Kim, *Anal. Chem.*, 2012, **84**, 1026–1033.
34 V. D'Atri, M. Porrini, F. Rosu and V. Gabelica, *J. Mass Spectrom.*, 2015, 50.
35 S. Warnke, J. Seo, J. Boschmans, F. Sobott, J. H. Scrivens, C. Bleiholder, M. T. Bowers, S. Gewinner, W. Schöllkopf, K. Pagel and G. von Helden, *J. Am. Chem. Soc.*, 2015, **137**, 4236–4242.
36 R. E. Johnson, *Encycl. Phys. Sci. Technol.*, 1987, **2**, 224–251.
37 T. Wyttenbach, C. Bleiholder, S. E. Anderson and M. T. Bowers, *Mol. Phys.*, 2015, 1–6.
38 T. Wyttenbach, C. Bleiholder and M. T. Bowers, *Anal. Chem.*, 2013, **85**, 2191–2199.
39 P. Ganguly, T. D. Do, L. Larini, N. E. LaPointe, A. J. Sercel, M. F. Shade, S. C. Feinstein, M. T. Bowers and J.-E. Shea, *J. Phys. Chem. B*, 2015, **119**, 4582–4593.
40 B. Delaunay, *Bull. Académie Sci. URSS Cl. Sci. Mathématiques Nat.*, 1934, **6**, 793–800.
41 C. B. Barber, D. P. Dobkin and H. T. Huhdanpaa, *ACM Trans Math. Softw.*, 1996, **22**, 469–483.
42 W. E. Lorensen and H. E. Cline, *Comput. Graph.*, 1987, **21**, 163–169.
43 M. Kazhdan, M. Bolitho and H. Hoppe, in *Proceedings of the fourth Eurographics symposium on Geometry processing*, 2006, vol. 7.
44 R. Zope, T. Baruah, M. Pederson and B. Dunlap, *Phys. Rev. B: Condens. Matter*, 2008, 77.
45 H. A. Lorentz, *Ann. Phys.*, 1881, **248**, 127–136.
46 D. Berthelot, *C.R. Hebd. Séances Acad. Sci.*, 1898, **126**, 1703–1855.
47 M. F. Sanner, A. J. Olson and J.-C. Spehner, *Biopolymers*, 1996, 305–320.